International Journal of Heat and Mass Transfer 67 (2013) 118–130

Contents lists available at ScienceDirect

International Journal of Heat and Mass Transfer

journal homepage: www.elsevier.com/locate/ijhmt

An investigation of effects of heights and a length on natural convection of three dimensional parallel plates with a heated bottom surface by a CUDA computation platform

Wu-Shung Fu *, Shang-Hao Huang, Wei-Hsiang Wang

Department of Mechanical Engineering, National Chiao Tung University, Hsinchu 30010, Taiwan, ROC

ARTICLE INFO

Article history:
Received 21 February 2013
Received in revised form 9 July 2013
Accepted 9 July 2013
Available online 29 August 2013

Keywords:
Natural convection
Horizontal parallel plates
Heated bottom surface
CUDA

ABSTRACT

Effects of heights and a length on natural convection of three dimensional parallel plates with a heated bottom surface are investigated numerically. The compressibility of fluid induced by a high temperature difference is taken into consideration for simulating more realistic situations, and then the Boussinesq assumption is not necessary to be adopted. Methods of the Roe scheme, preconditioning and dual time stepping matching the method of LUSGS are simultaneously used to solve the compressible flow problem. Non-reflecting boundary conditions are held on apertures to prevent reflections from apertures induced by pressure waves. A CUDA computational platform is used to economize massive computing time. Under a low height case, the flow field is restricted by the shear force caused by the low height and displays a stable situation. Oppositely, under a high height case the flow field indicates active behaviors and an irregular situation is observed.

1. Introduction

A subject of natural convection of three dimensional parallel plates with a heated bottom surface has attracted lots of attention in both practical applications and academic studies due to its importance to wide kinds of physical phenomena. In practical applications, this subject can be observed in many thermal equipment, such as energy storage equipment, solar collector, liquid crystal growth chamber. As for in the academic study, except unsteady behaviors, another interesting characteristic of the Rayleigh–Benard convection can also be found out. Studies of a numerical simulation [1,2] and a model analysis [3,4] were then investigated. An interaction between forces of a viscous force and the buoyancy force is recognized to dominate the occurrence of Rayleigh–Benard convection. Also, that boundary conditions have deep influence on phenomena of the Rayleigh–Benard convection is well-known. In the above literature, an enclosure which is one of important geometries of this subject was assumed the physical model. The Boussinesq assumption is adopted to substitute the variation of the density of the fluid. Due to the situation of the enclosure completely surrounded by walls, phenomena of the variation of the Rayleigh–Benard convection were very active and examined in detail in the above literature, and remarkable results were achieved.

A heated bottom wall in parallel plates with open-ended apertures which is another important geometry of this subject is often assumed as the physical model as well, and was investigated by numerous studies [5–14]. However, because the existence of the opened-ended apertures causes fluids to flow into and out off the channel continuously that results in an unsteady phenomenon easily occurring, but the phenomenon of the Rayleigh–Benard convection being relatively less found out and discussed. As for the treatment of boundary conditions at the opened-ended apertures, the enough length for satisfying a fully developed flow is adopted [15–17], and the enlarged computational domain is usually used by the far field boundary conditions [18–23]. However, existence of a pressure difference at the apertures would lead acoustic waves caused by the compressibility of fluid to reflect from the aperture, and then the low speed compressible flow in parallel plates will be polluted by the reflections of acoustic waves. As well, setting the enlarged computational domain outside the opened-ended apertures causes extra computational time and memory to be added. A preliminary study [24] of this work adopted the model of parallel plates with non-reflecting boundary conditions at open-ended apertures to investigate the subject. In this study, in an initial status cooling fluids were sucked from surroundings and flowed into the channel, and a pair of T-shape roll cells which are like the Rayleigh–Benard convection and a kind of intermediate product were observed. Finally the flow became unsteady when the bottom wall

* Corresponding author. Address: Department of Mechanical Engineering, National Chiao Tung University, 1001 Ta Hsueh Road, Hsinchu 30056, Taiwan, ROC. Tel.: +886 3 5712121x55110; fax: +886 3 5735065.
E-mail address: wsfu@mail.nctu.edu.tw (W.-S. Fu).

0017-9310/$ - see front matter © 2013 Elsevier Ltd. All rights reserved.
http://dx.doi.org/10.1016/j.ijheatmasstransfer.2013.07.030

Nomenclature

A	area (m^2)
d	width of the plate (m)
e	internal energy (J/kg)
g	acceleration of gravity (m/s^2)
h	height of the plate (m)
k	thermal conductivity (W/m K)
k_0	surrounding thermal conductivity (W/m K)
l	length of the plate (m)
Nu_x	local Nusselt number defined in Eq. (28) $Nu_x = \frac{h}{k_0(T_h - T_c)}\left[k(T)\frac{\partial T}{\partial y}\right]$
$\overline{Nu}_x$	time average local Nusselt number defined in Eq. (29) $\overline{Nu}_x = \frac{1}{t}\int_t Nu_x dt$
$\overline{Nu}_A$	area average local Nusselt number defined in Eq. (31) $\overline{Nu}_A = \frac{1}{d\cdot l}\int_d\int_l Nu_x dxdz$
$\bar{Nu}$	average Nusselt number defined in Eq. (32) $\bar{Nu} = \frac{1}{d\cdot l}\int_d\int_l \overline{Nu}_x dxdz$
P	pressure (Pa)
P_0	surrounding pressure (Pa)
Pr	Prandtl number
R	gas constant (J/kg/K)
R^*	length ratio $R^* = \frac{l}{h}$
Ra	Rayleigh number defined in Eq. (26) $Ra = \mathrm{Pr}\frac{g\rho_0^2(T_h - T_c)h^3}{T_0\mu(T)^2}$
Ra^*	modified Rayleigh number defined in Eq. (27) $Ra^* = Ra \times \frac{l}{h}$
Re	Reynolds number
t	time (s)
T	temperature (K)
T_0	initial temperature in the physical model (298.05 K)
T_c	temperature of surroundings (298.05 K)
T_h	temperature of heat surface (K)
u, v, w	velocities in x, y and z directions (m/s)
U, V, W	dimensionless velocities $U = \frac{u}{\sqrt{Ra^*}\frac{\alpha}{h}}, V = \frac{v}{\sqrt{Ra^*}\frac{\alpha}{h}}, W = \frac{w}{\sqrt{Ra^*}\frac{\alpha}{h}}$
x, y, z	Cartesian coordinates (m)
X, Y, Z	dimensionless Cartesian coordinates $X = \frac{x}{l_3}$, $Y = \frac{y}{l_3}$ and $Z = \frac{z}{l_3}$

Greek symbols

α	thermal diffusivity rate (m^2/s)
ρ	density (kg/m^3)
ρ_0	surrounding density (kg/m^3)
μ	viscosity (N s/m^2)
μ_0	surrounding viscosity (N s/m^2)
γ	specific heat ratio

was completely installed by a heated surface. However, as the length of the heated surface was shorter than a half of the bottom surface length, the T-shape roll cell was no longer observed, and finally the flow became a quasi-steady or a steady flow. The reason is suggested as that the shorter heated bottom surface provides the less buoyancy force and it is difficult to compete with the horizontal viscous force. As for the influences of different heights and a longer heated bottom surface on the subject mentioned above are scarcely investigated.

Therefore, two different heights which are separately lower and higher than the height of [24] and a longer length which is two times as long as the heated bottom surface length of [24] are taken into consideration to examine the interaction of the viscous and buoyancy forces and the growth of the T-shape roll cell, respectively. For simulating the subject more realistically, the Boussinesq assumption is not adopted, and instead, the compressibility of the fluid is considered. The buoyancy force is then to vary with the heating process and exerts on the fluid from weakly to strongly. The time needed for computation and data acquisition is extremely huge, and then an effective method of a CUDA computation [24] is needed for executing parallel computations. Solution methods of the Roe [25], preconditioning [26] and dual time stepping [27] for solving a low speed compressible fluid flow in a transient state are combined together. As well, a modified method of the non-reflecting boundary condition [28] is used to treat the reflection of pressure wave at the apertures of parallel plates. The results show that under a low height situation the parallel plates are like narrow parallel plates, and then the viscous force dominates the flow field that easily causes the flow field to become a steady state. Oppositely, under a high height situation the parallel plates are like wide parallel plates, and then the more active buoyancy force naturally dominates the flow field that causes the flow field to be an unsteady state. Unexpectedly, the T-shape roll cell cannot be observed. As for the results of the longer heated bottom surface, two pairs of the T-shape roll cells are found out during a transient status. The height adopted in [24] seems to be an appropriate height to produce the T-shape roll cells.

2. Physical model

A physical model of three dimensional horizontal parallel plates is indicated in Fig. 1. The length and height of the physical model are l and h, respectively. The bottom plate is a heated wall and the temperature of the heated wall is T_h and equal to 700 k. The top plate is adiabatic. The width of the physical model is d, and the direction of gravity is downward. Boundary conditions at both apertures are non-reflecting conditions and both sides of the width are periodic conditions. The pressure and temperature of the outside of parallel plates are 101,300 Pa and 298 K, respectively.

For facilitating the analysis, the following assumptions are made.

1. The work fluid is ideal gas and follows the equation of state of an ideal gas.
2. Magnitudes of gradients of density and pressure on the whole surfaces in the normal direction are zero.
3. Radiation heat transfer is neglected.

The governing equations are expressed as follows.

$$\frac{\partial U}{\partial t} + \frac{\partial F}{\partial x} + \frac{\partial G}{\partial y} + \frac{\partial H}{\partial z} = S \tag{1}$$

and the equation of state of an ideal gas is used.

$$P = \rho RT \tag{2}$$

The terms included in U, F, G, H and S are separately shown in the following equations.

$$U = \begin{bmatrix} \rho \\ \rho u \\ \rho v \\ \rho w \\ \rho E \end{bmatrix} \tag{3}$$

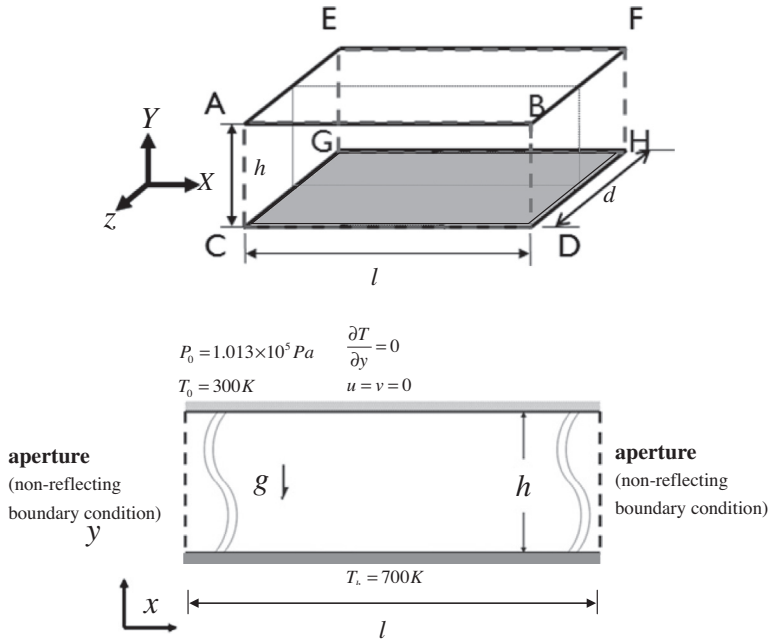

Fig. 1. Physical model.

$$
F = \begin{bmatrix} \rho u \\ \rho u^2 + P - \tau_{xx} \\ \rho uv - \tau_{xy} \\ \rho uw - \tau_{xz} \\ \rho Eu + Pu - k\frac{\partial T}{\partial x} - u\tau_{xx} - v\tau_{xy} - w\tau_{xz} \end{bmatrix}
$$

$$
G = \begin{bmatrix} \rho v \\ \rho uv - \tau_{yx} \\ \rho v^2 + P - \tau_{yy} \\ \rho vw - \tau_{yz} \\ \rho Ev + Pv - k\frac{\partial T}{\partial y} - u\tau_{yx} - v\tau_{yy} - w\tau_{yz} \end{bmatrix}
$$

$$
H = \begin{bmatrix} \rho w \\ \rho uw - \tau_{zx} \\ \rho vw - \tau_{zy} \\ \rho w^2 + P - \tau_{zz} \\ \rho Ew + Pw - k\frac{\partial T}{\partial z} - u\tau_{zx} - v\tau_{zy} - w\tau_{zz} \end{bmatrix}
$$

$$
S = \begin{bmatrix} 0 \\ 0 \\ -(\rho - \rho_0)g \\ 0 \\ -(\rho - \rho_0)gv \end{bmatrix} \tag{4}
$$

Sutherland's law is adopted to evaluate the viscosity and thermal conductivity shown as follows.

$$
\mu(T) = \mu_0 \left(\frac{T}{T_0}\right)^{\frac{2}{3}} \frac{T_0 + 110}{T + 110} \tag{5}
$$

$$
k(T) = \frac{\mu(T)\gamma R}{(\gamma - 1)\mathrm{Pr}} \tag{6}
$$

in which

$$
E = \frac{P}{\rho(\gamma - 1)} + \frac{1}{2}(u^2 + v^2 + w^2) \tag{7}
$$

$\rho_0 = 1.1842\ \mathrm{kg/m^3}, g = 9.81\ \mathrm{m/s^2}$,
$\mu_0 = 1.85 \times 10^{-5}\ \mathrm{Ns/m^2}, T_0 = 298.05\ \mathrm{K}$,
$\gamma = 1.4, R = 287\ \mathrm{J/kg/K}, \mathrm{Pr} = 0.72$.

3. Numerical method

The Roe scheme [25] and preconditioning method [26] are used to solve the governing equations of a compressible flow shown in Eq. (1). Also, the method of dual time stepping is added to calculate transient states. And Eq. (8) can be obtained.

$$
\Gamma\frac{\partial U_p}{\partial \tau} + \frac{\partial U}{\partial t} + \frac{\partial F}{\partial x} + \frac{\partial G}{\partial y} + \frac{\partial H}{\partial z} = S \tag{8}
$$

where τ is an artificial time, t is a physical time. Γ is a preconditioning matrix proposed by Weiss and Smith [26] and U_p is a primitive form of $[\rho, \rho u, \rho v, \rho w, \rho e]^T$. Discretization of Eq. (8) is executed. The terms of $\frac{\partial U_p}{\partial \tau}$ and $\frac{\partial U}{\partial t}$ are differentiated by a first-order forward difference and a second-order backward difference, respectively, and the terms of $\frac{\partial F}{\partial x}$, $\frac{\partial G}{\partial y}$, and $\frac{\partial H}{\partial z}$ are differentiated by a central difference, the following equation can be obtained.

$$
\begin{aligned}
&\Gamma\frac{U_p^{k+1} - U_p^k}{\Delta\tau} + \frac{3U^{n+1} - 4U^n + U^{n-1}}{2\Delta t} + \frac{1}{\Delta x}\left(F^{k+1}_{i+\frac{1}{2},j,k} - F^{k+1}_{i-\frac{1}{2},j,k}\right) \\
&+ \frac{1}{\Delta y}\left(G^{k+1}_{i,j+\frac{1}{2},k} - G^{k+1}_{i,j-\frac{1}{2},k}\right) + \frac{1}{\Delta z}\left(H^{k+1}_{i,j,k+\frac{1}{2}} - H^{k+1}_{i,j,k-\frac{1}{2}}\right) = S
\end{aligned} \tag{9}
$$

The terms of U^{k+1} and F^{k+1} in Eq. (9) are necessary to be linearized and expressed as follows.

$$
U^{k+1} = U^k + M\Delta U_p \tag{10}
$$

in which $M = \frac{\partial U}{\partial U_p}$ and $A_p = \frac{\partial F^k}{\partial U_p}$

$$
F^{k+1} = F^k + A_p\Delta U_p \tag{11}
$$

where $A_p = \frac{\partial F}{\partial U_p}$ is the flux Jacobian and the same methods for $B_p = \frac{\partial G}{\partial U_p}$ and $C_p = \frac{\partial H}{\partial U_p}$ are used in linearization of G^{k+1} and H^{k+1}, respectively.

To substitute Eqs. (10) and (11) into Eq. (9), the following equation is derived.

$$
\left[\frac{I}{\Delta\tau} + \Gamma^{-1}M\frac{3}{2\Delta t} + \Gamma^{-1}\left(\delta_x A_p^k + \delta_y B_p^k + \delta_z C_p^k\right)\right]\Delta U_p = \Gamma^{-1}R^k \tag{12}
$$

where δ_x, δ_y, and δ_z are central-difference operators and $R^k = S - (\frac{3U^k - 4U^n + U^{n-1}}{2\Delta t}) - (\delta_x F^k + \delta_y G^k + \delta_z H^k)$

The solver of the following Eq. (13) is the LUSGS implicit method proposed by Yoon and Jamesont [29].

$$A_p = \Gamma^{-1}A_p^k$$

$$B_p = \Gamma^{-1}B_p^k \tag{13}$$

$$C_p = \Gamma^{-1}C_p^k$$

Eq. (12) can be rearranged as follows.

$$(L + D + U)\Delta U_p = \Gamma^{-1}R^k \tag{14}$$

where

$$\left.\begin{aligned} L &= -\left[\tfrac{1}{\Delta x}\left(A_p^+\right)_{i-1,j,k} + \tfrac{1}{\Delta y}\left(B_p^+\right)_{i,j-1,k} + \tfrac{1}{\Delta z}\left(C_p^+\right)_{i,j,k-1}\right] \\ D &= \tfrac{1}{\Delta t} + \Gamma^{-1}M\tfrac{3}{2\Delta t} + \left\{\tfrac{1}{\Delta x}\left[\left(A_p^+\right)_{i,j,k} - \left(A_p^-\right)_{i,j,k}\right] + \tfrac{1}{\Delta y}\left[\left(B_p^+\right)_{i,j,k} - \left(B_p^-\right)_{i,j,k}\right] + \tfrac{1}{\Delta z}\left[\left(C_p^+\right)_{i,j,k} - \left(C_p^-\right)_{i,j,k}\right]\right\} \\ U &= \left[\tfrac{1}{\Delta x}\left(A_p^-\right)_{i+1,j,k} + \tfrac{1}{\Delta y}\left(B_p^-\right)_{i,j+1,k} + \tfrac{1}{\Delta z}\left(C_p^-\right)_{i,j,k+1}\right] \end{aligned}\right\} \tag{15}$$

As for the computation of $R^k = S - \left(\frac{3U^k - 4U^n + U^{n-1}}{2\Delta t}\right) - \left(\delta_x F^k + \delta_y G^k + \delta_z H^k\right)$ in the right hand side (RHS) of Eq. (12), the terms included in F shown in Eq. (4) based on Cartesian coordinates can be divided into two parts. One is the inviscid term $F_{inviscid}$ and the other is the viscous term $F_{viscous}$.

$$F = F_{inviscid} + F_{viscous} = \begin{Bmatrix} \rho u \\ \rho u^2 + p \\ \rho u v \\ \rho u w \\ \rho\left(e + \frac{V^2}{2}\right)u + pu - k\frac{\partial T}{\partial x} \end{Bmatrix} - \begin{Bmatrix} 0 \\ \tau_{xx} \\ \tau_{xy} \\ \tau_{xz} \\ +u\tau_{xx} + v\tau_{xy} + w\tau_{xz} \end{Bmatrix} \tag{16}$$

The upwind difference scheme developed by Roe [25] is employed in discretization of the term of $F_{inviscid}$ at the interface cells $(i+\frac{1}{2})$ and expressed as follows at a low Mach number situation.

$$F_{inviscid,i+\frac{1}{2}} = \frac{1}{2}(F_R + F_L) - \frac{1}{2}|\Gamma^{-1}AM|\Delta U_P \tag{17}$$

The third-order MUSCL scheme proposed by Abalakin et al. [30] is used to compute the term of $F_{inviscid}$. And a second central difference is adopted to calculate the magnitudes of the viscous terms and the related derivations are indicated as follows.

$$\frac{\partial u}{\partial x} = \frac{u_{i-1} - u_{i+1}}{2\Delta x} + o(\Delta x) \tag{18}$$

And the same methods for G and H are used, respectively.

On the adiabatic surface, the boundary conditions are

$$\begin{aligned} P(i,0,k) &= P(i,1,k) \\ u(i,0,k) &= -u(i,1,k) \\ v(i,0,k) &= -v(i,1,k) \\ w(i,0,k) &= -w(i,1,k) \\ T(i,0,k) &= T(i,1,k) \end{aligned} \tag{19}$$

$$\begin{aligned} P(i,ny+1,k) &= P(i,ny,k) \\ u(i,ny+1,k) &= u(i,ny,k) \\ v(i,ny+1,k) &= v(i,ny,k) \\ w(i,ny+1,k) &= w(i,ny,k) \\ T(i,ny+1,k) &= T(i,ny,k) \end{aligned} \tag{20}$$

On the heated surface, the boundary conditions are

$$\begin{aligned} P(i,0,k) &= P(i,1,k) \\ u(i,0,k) &= -u(i,1,k) \\ v(i,0,k) &= -v(i,1,k) \\ w(i,0,k) &= -w(i,1,k) \\ T(i,0,k) &= 2T_h - T(i,1,k) \end{aligned} \tag{21}$$

where T_h is the wall temperature.

0 indicates the ghost cell and 1 indicates the cell closest to the wall.

As for the boundary conditions at the apertures of parallel plates, in order to avoid a low speed compressible flow in parallel plates to be polluted by the reflections of acoustic waves, the non-reflecting boundary conditions are then necessarily used at the apertures of parallel plates.

In a high speed compressible flow condition, the method of LODI (local one dimensional inviscid relations) proposed by Poinsot and Lele [31] was suitably adopted for determining the non-reflecting boundary conditions at the apertures of the channel. However, a preconditioning matrix is not used in the above method that causes the method to be not available for determining the non-reflecting boundary conditions at the apertures under a low speed compressible flow. As a result, the modification of the above method [28] is adopted for resolving the non-reflection boundary conditions under an extremely low speed compressible flow.

Along the Z direction, periodic conditions are used, and then the boundary conditions of surfaces of ABCD and EFGH shown in Fig. 1 can be expressed as the following equations, respectively.

$$\begin{aligned} P(i,j,0) &= P(i,j,nz) \\ u(i,j,0) &= u(i,j,nz) \\ v(i,j,0) &= v(i,j,nz) \\ w(i,j,0) &= w(i,j,nz) \\ T(i,j,0) &= T(i,j,nz) \end{aligned} \tag{22}$$

$$\begin{aligned} P(i,j,nz+1) &= P(i,j,1) \\ u(i,j,nz+1) &= u(i,j,1) \\ v(i,j,nz+1) &= v(i,j,1) \\ w(i,j,nz+1) &= w(i,j,1) \\ T(i,j,nz+1) &= T(i,j,1) \end{aligned} \tag{23}$$

0 indicates the cell at the ABCD surface and $nz + 1$ indicates the cell at the EFGH surface.

A procedure calculating the equations mentioned above is briefly described as follows.

(1) Assign the initial conditions of pressure, velocities and temperatures.
(2) Use the MUSCL method to calculate Eq. (12) to obtain the magnitude of ΔU_p.
(3) Substitute the magnitude of ΔU_p into Eq. (17) and use the Roe method to calculate the magnitudes of inviscid terms of $F_{inviscid}$.
(4) Calculate Eq. (18) to obtain the magnitudes of viscous terms and substitute in Eq. (16).
(5) Solve U_p^{k+1}.

$$U_p^{k+1} = U_p^k + \Delta U_p^k \tag{24}$$

(6) Calculate Eq. (9) and examine the convergence of the iterational computation of U_p^{k+1}. Repeat (2)–(5) until $\frac{U_p^{k+1} - U_p^k}{\Delta\tau} < \varepsilon$, $\varepsilon = 10^{-3}$.

The time of computation and date acquisition is extremely huge, and an effective method of a CUDA computation platform

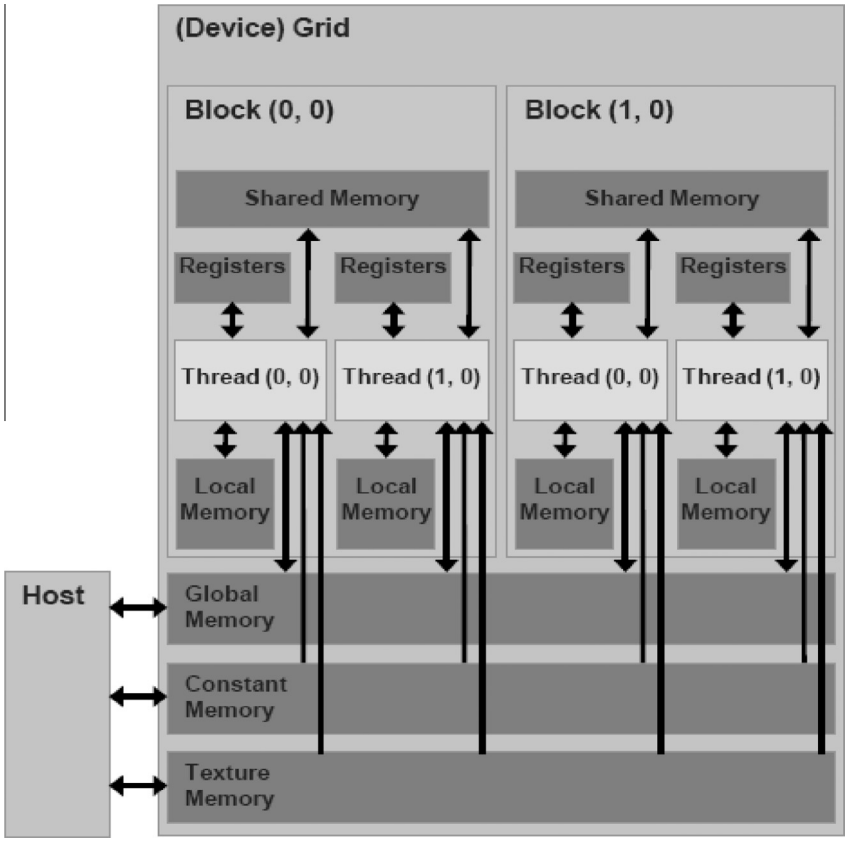

Fig. 2. Schematic diagram of CUDA platform [32].

is then used for executing parallel computation. The main function of the CUDA computation platform [14], which is a kind of integrated technique developed by NVIDIA company, is to integrate the performance of a GPU (Graphics Processing Unit) arrayed in a video card installed in a host computer to a numerical parallel computation processor executed in the host computer.

A brief description of usage of the CUDA is indicated as follows. Three steps have been executed and Fig. 2 is the schematic diagram. The first step is that the data are moved from the memory of the host to the memory in the graphic hardware. Then the GPU is utilized to compute. The general method of assigning numbers in three dimensional grids is a three dimensional matrix (i, j, k). However, it will be very complicated to move the data from the host to the graphic hardware if the three dimensional matrix is adopted. Therefore, it is necessary to transport the three dimensional matrix to the one dimensional matrix. Then, the data will be easy to be moved. The equation of transporting is showed in the following process.

$$\text{Device (assign numbers)} = \text{host}(i \times ny \times nz + j \times nz + k) \tag{25}$$

where nx, ny and nz are the numbers of grids in the x, y and z direction, respectively.

The second step is to parallel the program. The best advantage of the graphic hardware is that there are multiple cores in it to execute the computation. Then the program paralleling is absolutely necessary.

The third step is to move the results computed by GPUs from the graphic hardware to the host and transform the one dimensional matrix to the original three dimensional matrix. Performance tests of CUDA computation platforms are similar to those of [24].

4. Results and discussion

The height of parallel plates is usually regarded as a characteristic length when the Rayleigh number is used in a parallel plates problem and defined as follows.

$$Ra = \Pr \frac{g\rho_0^2 (T_h - T_c) h^3}{T_0 \mu(T)^2} \tag{26}$$

However, the length of the heated bottom wall affects heat transfer phenomena remarkably. In order to highlight the influence of the length of the heated wall, a modified Rayleigh number Ra^* is newly defined in the following equation.

$$Ra^* = Ra \times \frac{l}{h} \tag{27}$$

In this study, relative to the scales of the previous study [24] two different heights and a different length of the heated wall are considered, and three different magnitudes of $R = \frac{l}{h}$ are shown as follows, respectively.

$\frac{11}{2}(Ra^* = 2.18 \times 10^6)$, $\frac{11}{6}(Ra^* = 1.95 \times 10^7)$ and $\frac{22}{4}(Ra^* = 1.73 \times 10^7)$.

The grid distribution of $250 \times 160 \times 10$ is selected according to the previous study [24]. The definitions of local and time-averaged local Nusselt numbers of Nu_x and $\overline{Nu}_x$ are expressed as follows, respectively.

$$Nu_x = \frac{h}{k_0(T_h - T_c)} \left[k(T) \frac{\partial T}{\partial y} \right] \tag{28}$$

$$\bar{Nu}_x = \frac{1}{t} \int_t Nu_x dt \tag{29}$$

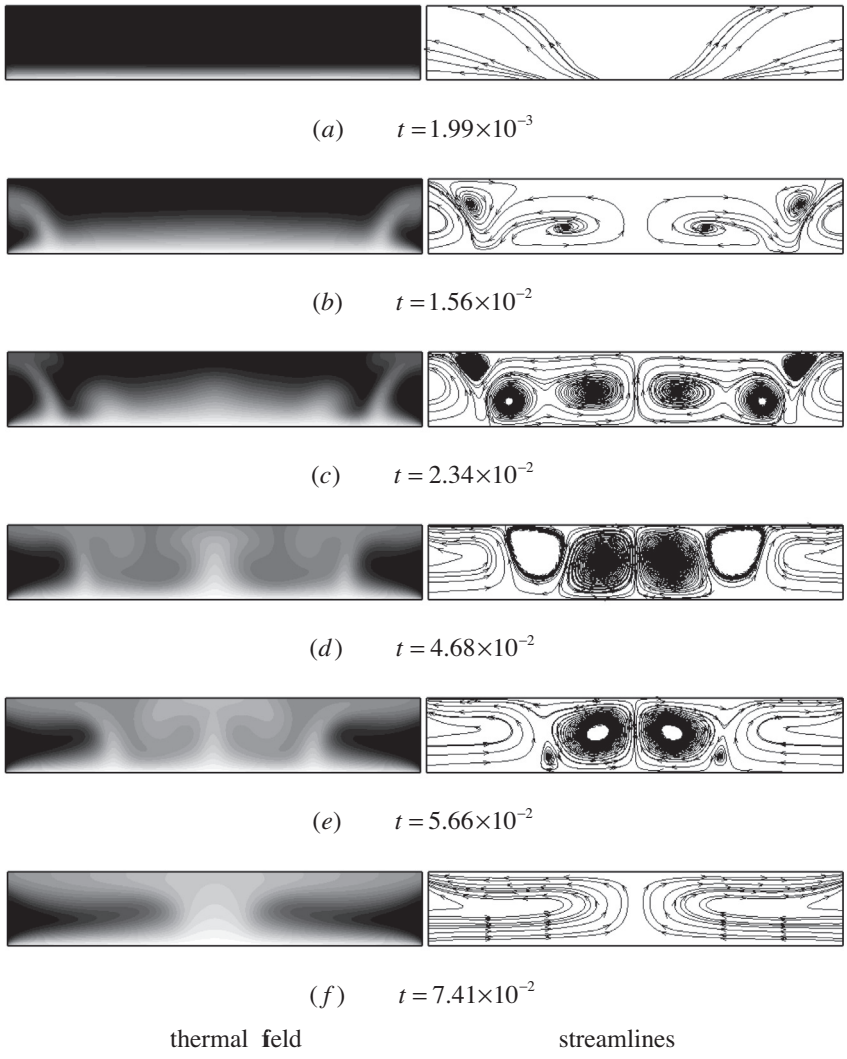

Fig. 3. Histories of development of thermal field and streamlines under $Ra^* = 2.18 \times 10^6$.

In Fig. 3, histories of development of thermal fields and streamlines are separately indicated under $Ra^* = 2.18 \times 10^6$ situation. The height is a half of [24]. The darker the color is, the lower the temperature displays. At the initial stage ($t = 1.99 \times 10^{-3}$), heat conduction mode dominates the heat transfer phenomenon, and then thermal layers distributed on the whole heated bottom surface are uniform. Fluids close to the heated bottom surface are heated and expanded, so via apertures fluids are discharged into surroundings. In the next stage ($t = 1.56 \times 10^{-2}$), because the height of parallel plates is low, light heated fluids close to the apertures are first raised and flow out off the parallel plates. Meanwhile cooling fluids are sucked from surroundings and flow into the parallel plates, but they are restricted in the outside region of the ascending fluids mentioned above. Therefore, close to the apertures there are two dark zones surrounded by two light belts to be observed. This phenomenon causes the temperatures of the fluids in the region between the two light belts to be increased gradually. Accompanied with the increment of the temperatures of fluids, the fluids start to form circulations by themselves. As the time passes, the light region in which the temperature is increased is enlarged gradually because of the activity of natural convection mode. The circulations merge into two big pairs of circulations shown in Fig. 3(d). Afterward, the heated fluids ascend and impinge on the top wall and start to flow out off parallel plates. Then cooling fluids sucked from surroundings begin to increase and contract the space filled with the heated fluids. Finally, the ascending heated fluids concentrate in the central region, and the circulations are completely eliminated. The thermal and flow fields become a symmetrically steady situation shown in Fig. 3(f). Due to the low height of parallel plates, the strength of viscous shear force is relatively apparent, and then the strength of natural convection seems to have difficulty to produce the T-shape roll cell which found out in [24].

Shown in Fig. 4, the height of parallel plates is increased and two times as high as that of [24]. This situation means that natural convection plays a more active role and the strength of it becomes stronger. In Fig. 4(a), at an initial stage heat conduction mode is dominant, and then fluids which are expanded by the heat from of the heated bottom wall are discharged to surroundings. Thermal layers are uniformly distributed on the heated bottom surface which is similar to that shown in Fig. 3(a). However, as the time passes and the strong strength of natural convection directly causes heated fluids in the central region to ascend and flow outward. The T-shape roll cell is unable to be formed in time and not observed. The T-shape roll cell shown in [24] indicated the ascending fluids separately to flow outward and inward that means the strength of cooling fluids which are sucked from surroundings due to natural convection to be not strong enough to

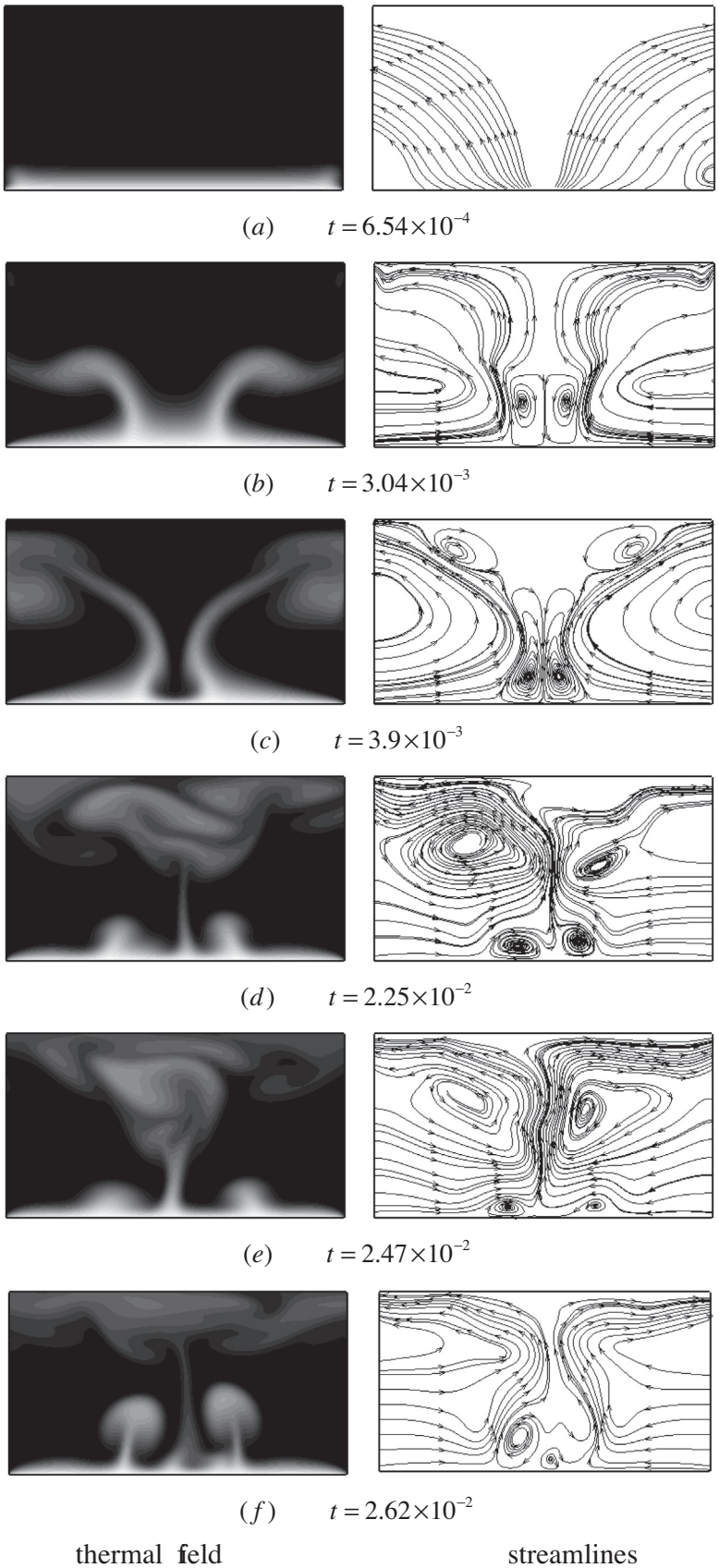

Fig. 4. Histories of development of thermal field and streamlines under $Ra^* = 1.95 \times 10^7$.

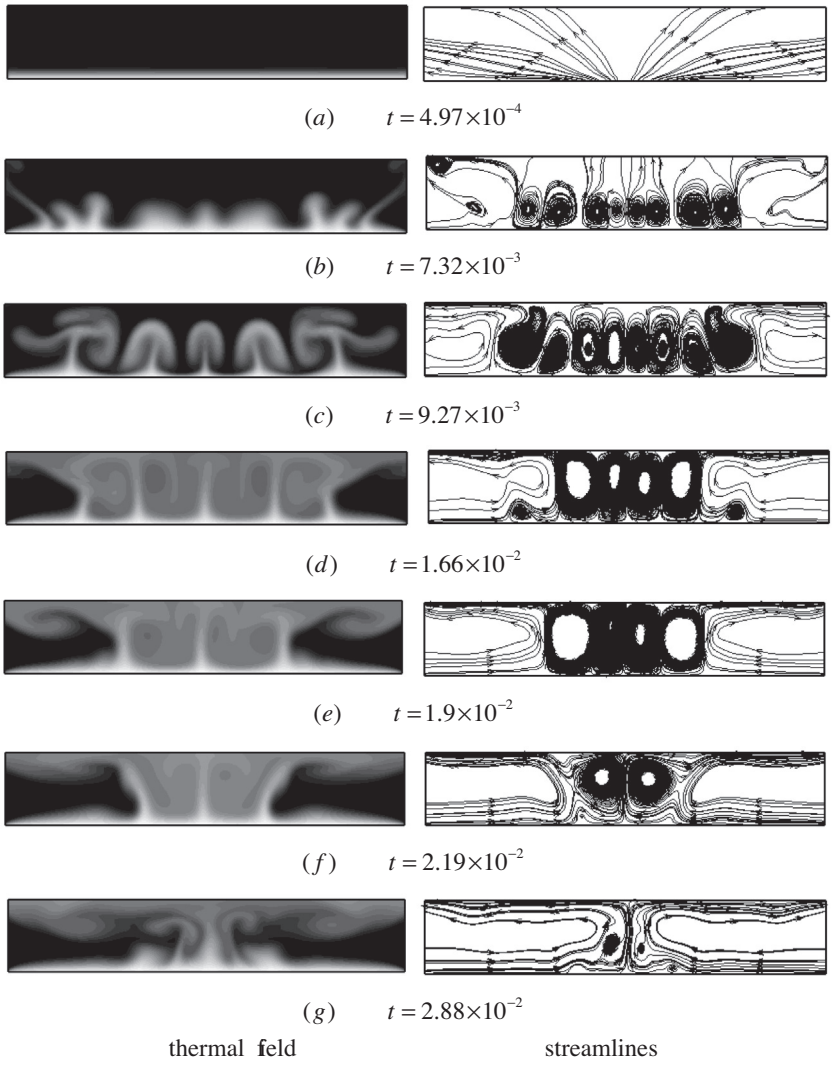

Fig. 5. Histories of development of thermal field and streamlines under $Ra^* = 1.73 \times 10^7$.

lead the ascending fluids to flow outward exclusively. Except the appearance of two large circulations caused by the ascending fluids mentioned above, two small closed circulations in the low central region induced by the two large circulations are observed. Afterward, the two big circulations continuously grow and suppress the two small closed circulations that forces the two new small closed circulations to be released and flow outward along the edges of the big circulations. Finally, the two big circulations contact with each other and mutually squeeze. Although the two small closed circulations are suppressed by the two big circulations, they still exist on the heated bottom surface. No small closed circulation existed and only two big swing circulations were observed at the final stage of [24]. The reason of the different phenomenon between this work and [24] is suggested as that the strength of natural convection of this work is stronger than that of [24]. The active strength of natural convection of this work in the central region easily produces ascending fluids, but the ascending fluids have no ability to push away the upper big circulations formed by the whole regions. As a result, the ascending fluids are permitted to form small closed circulations only. Because of the mutual squeeze of the two big circulations, the situation of natural convection becomes unsteady and the strength of the closed small circulation varies inversely with the variation of the strength of the upper big circulation shown in Fig. 4(e). Due to easy accumulation of heat energy on the central bottom surface, sometimes the two small suppressed circulations are suddenly ejected from the bottom surface like a shape of mushroom.

In Fig. 5, the length of the heated bottom surface of this situation is two times as long as that of the previous study [24]. The height of both situations is the same. Since the heated bottom surface is long, cooling fluids sucked from surroundings are more difficult to flow into the central region directly in initial stages. As a result, shown in Fig. 5(b) based on the central region two pairs of high temperature convexes are observed symmetrically in the thermal field on both sides. Corresponding to the convexes, several circulations are formed. Afterward, at the corresponding locations of the convexes T-shape roll cells which were observed in [24] are indicated. The number of the convexes is larger than that of [24], because of the longer length of this study. As well, circulations grow bigger accompanied with the growth of T-shape roll cells. These phenomena are not observed in the above situations shown in Figs. 3 and 4. It implies that an appropriate ratio of the height to the length will cause the indication of the T-shape roll cell to appear in parallel plates. The Rayleigh–Benard convection indicated in the situation of the enclosure [1–4] is not found out in this study. It is reasoned as that the situation with open-ended

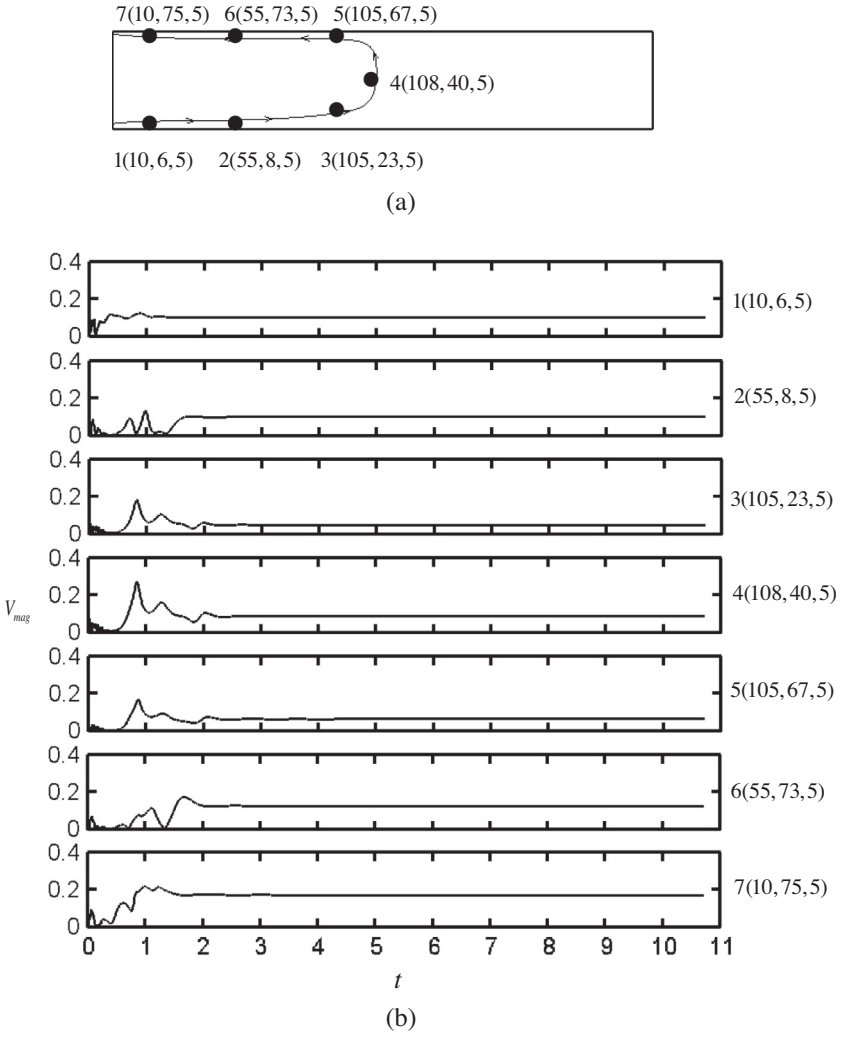

Fig. 6. Variations of local resultant velocity V_{mag} at different locations of a time average streamline under $Ra^* = 2.18 \times 10^6$.

apertures leads fluids to exchange interruptedly between the inside of parallel plates and surroundings. Then the permanent detention of fluids in their own circulations mentioned above becomes impossible, and the indication of the Rayleigh–Benard convection in parallel plates is hardly found out. The growth of the T-shape roll cell proceeds with a continuously heating process, and a mutual interference and mergence among the T-shape roll cells begin to be observed. The number of circulations begins to be decreased. Finally two big circulations are left, and two small closed circulations hide beneath the two big circulations to be found out that causes the situation to become an unsteady state. The height and length are separately lower and longer than those of Fig. 4, and then the two small closed circulations have no possibility to be ejected from the central bottom surface.

In Fig. 6, a time-averaged streamline close to both the top and bottom surfaces is indicated under the $Ra^* = 2.18 \times 10^6$ situation. Points of 1–7 from the inlet to outlet present corresponding locations on the streamline. Computational grids have difficulty to match points of 1–7 exactly, and then the closest computational grids corresponding to points of 1–7 are selected. Variations of resultant velocities with time at each point are shown in Fig. 6(b). The definition of the resultant velocity V_{mag} is expressed as follows.

$$V_{mag} = (U^2 + V^2 + W^2)^{\frac{1}{2}} \tag{30}$$

In duration of an initial stage, fluids in parallel plates are discharged into surroundings by heat conduction mode, and right after fluids are sucked from surroundings and flows into parallel plates by natural convection mode. As a result, the variation of the resultant velocity is apparent even though the magnitude of the resultant velocity is small. Accompanied with increment of time, natural convection gradually dominates the variations of thermal and flow fields. Due to the low height of parallel plates, the space for the development of natural convection is limited, and then the situation of natural convection becomes steady mentioned above. Therefore, after the initial stage the variation of the resultant velocity at each location is hardly found out.

In Fig. 7, the height of parallel plates is increased. The space for the development of natural convection is enlarged that causes active behaviors of natural convection to be induced. The location of point 1 is close to the aperture and fluids begin to be heated as they flow through this location. Then the influence of natural convection just begins that causes the variation of the resultant velocity to be slight. At the location of point 2, a vertical velocity induced by the buoyancy force becomes more remarkable than that at the location of point 1 that easily results in the variation of the resultant velocity at this location being more drastic than that at the location of point 1. The location of point 3 is in the central region that leads the resultant velocity to have an upward trend and naturally the variation of the thermal field to be slight. Consequently,

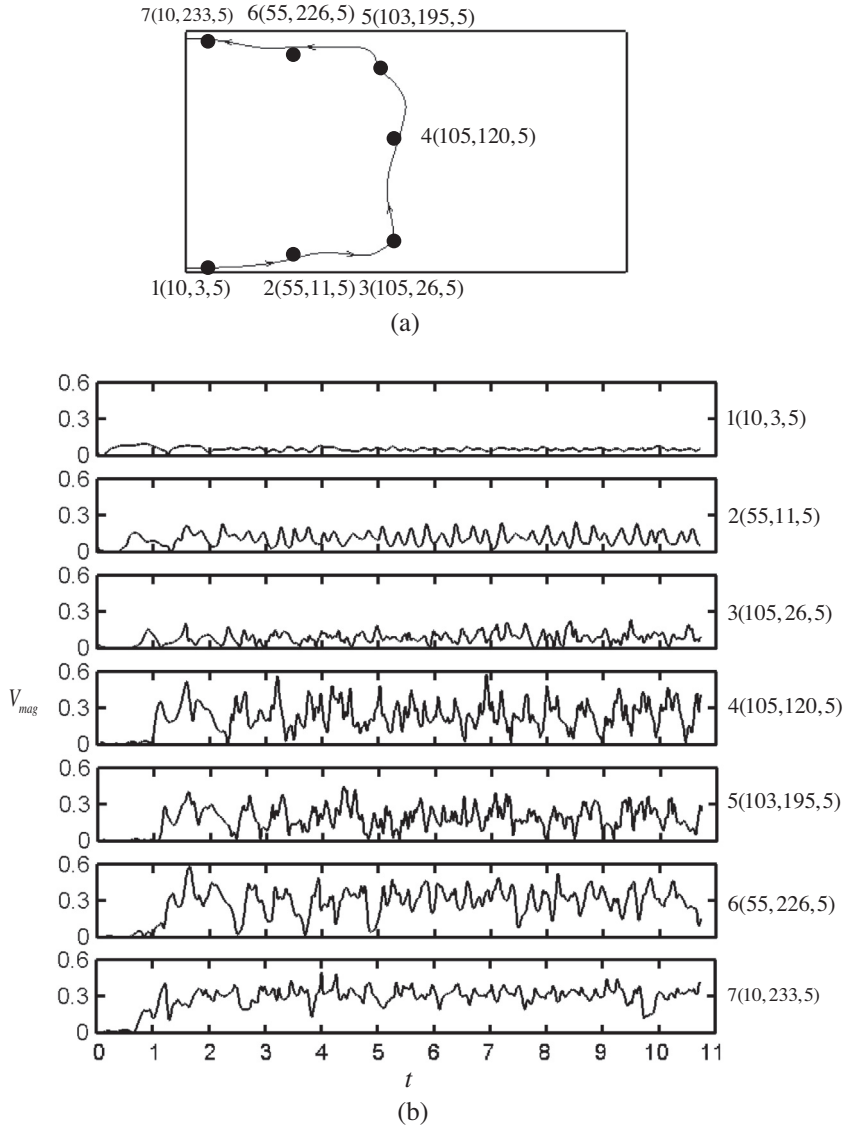

Fig. 7. Variations of local resultant velocity V_{mag} at different locations of a time average streamline under $Ra^* = 1.95 \times 10^7$.

the variation of the resultant velocity at this location is more stable than that at the location of point 2.

From point 4 to 7, the heating process is almost completed, then fluids possess more active behaviors. Except the indication of large magnitudes of resultant velocities, variations of resultant velocities at these locations are naturally apparent than those at the front locations mentioned above. The observation of the relatively small variation of the resultant velocity at the location of point 7 is caused by a viscous effect because of the short distance between the location and top surface.

In Fig. 8, due to the longer length of the heated bottom surface, cooling fluids sucked from surroundings absorb more heat energy that leads behaviors of fluids to become more active. Restrictive effects of the shear force caused by the top and bottom walls on behaviors of fluids are no longer dominant. Variations of the resultant velocity at each point are then more apparent than those shown in Fig. 6. But magnitudes of resultant velocities are generally smaller than those indicated in Fig. 7 reasoned by the smaller height adopted in this situation.

In Fig. 9, variations of instantaneous area-averaged Nusselt numbers on the *xz* plane with time are shown. The definition of the instantaneous area-averaged Nusselt number is expressed as follows.

$$\bar{Nu}_A = \frac{1}{d \cdot l} \int_d \int_l Nu_x dx dz \tag{31}$$

Naturally, the higher the height is, the larger the instantaneous area-averaged Nusselt is achieved. Under the situation of $Ra^* = 2.18 \times 10^6$, it is stable except the initial stage, then no variation of the instantaneous area-averaged Nusselt number is observed. Oppositely, under the situation of $Ra^* = 1.95 \times 10^7$, it is reveals an unstable state, then an irregular variation of the instantaneous area-averaged Nusselt number appears.

Shown in Fig. 10, there are variations of time-averaged local Nusselt numbers on the central cross section of the *xy* plane. A more larger space for the development of natural convection can be used under a higher height situation. As a result, large time-averaged local Nusselt numbers are achieved with the situation of the large Rayleigh number. In Fig. 4(e), two small closed circulations exist that causes two convexes of the time-averaged local Nusselt number to be indicated in the central region of the situation of $Ra^* = 1.95 \times 10^7$. Under the stable situation of

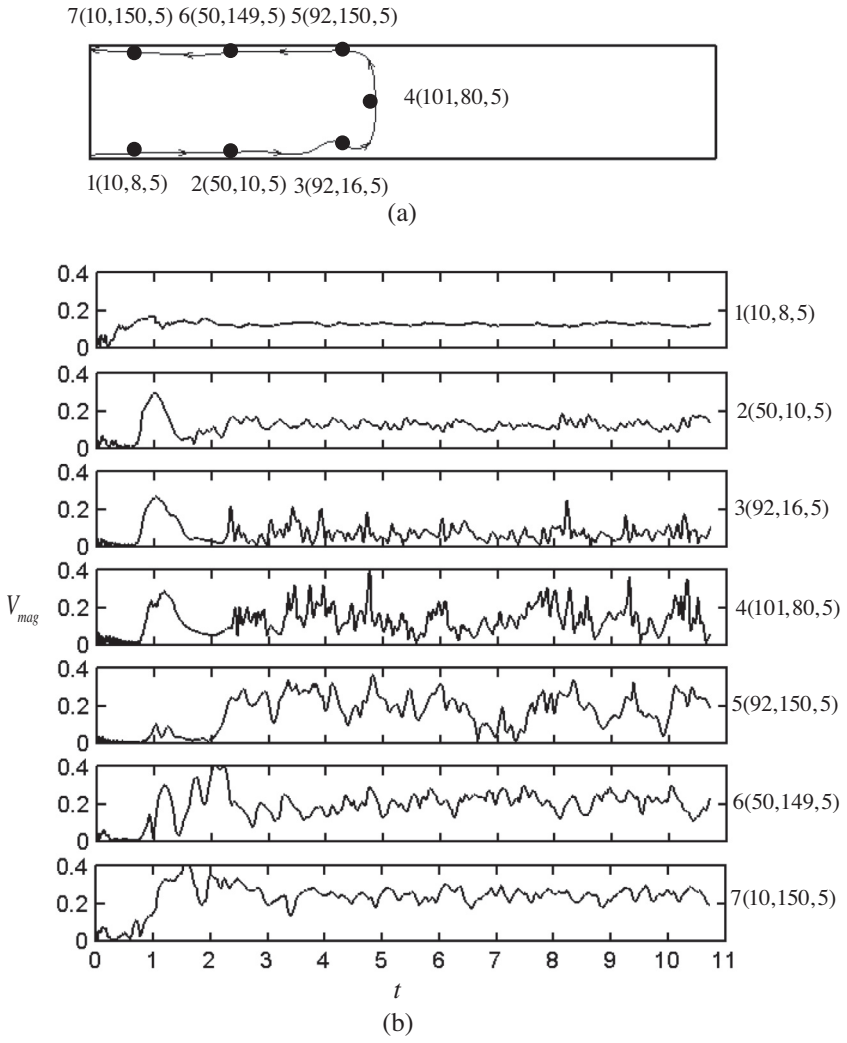

Fig. 8. Variations of local resultant velocity V_{mag} at different locations of a time average streamline under $Ra^* = 1.73 \times 10^7$.

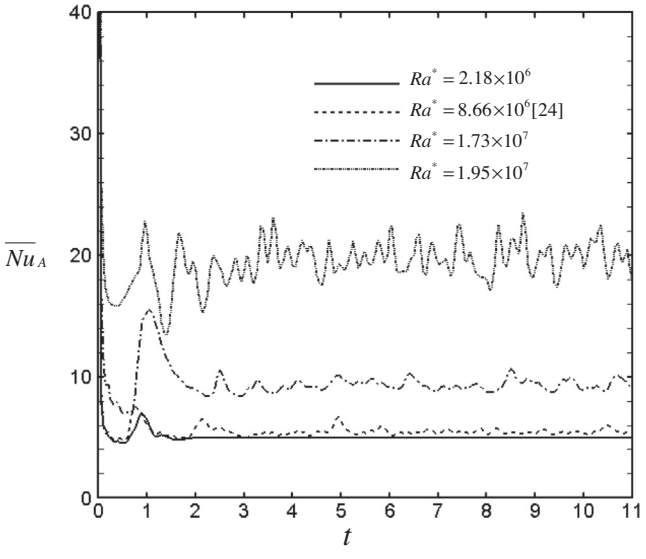

Fig. 9. Variations of instantaneous area-averaged Nusselt numbers with time.

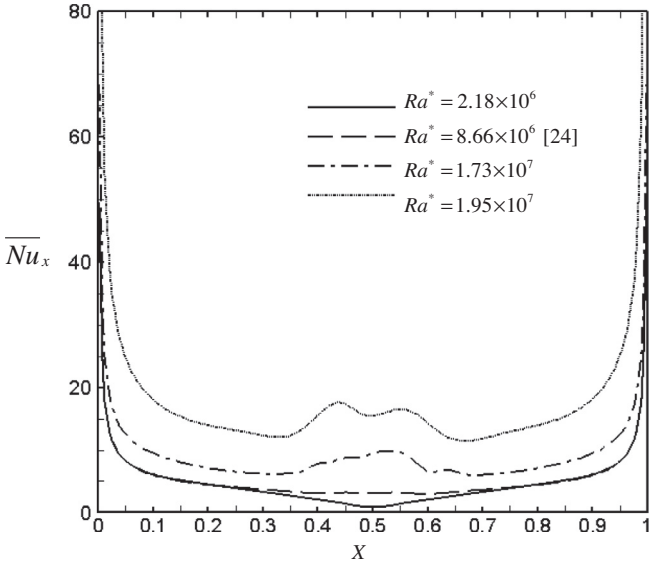

Fig. 10. Distributions of time-averaged local Nusselt numbers on the central cross section of the *xy* plane.

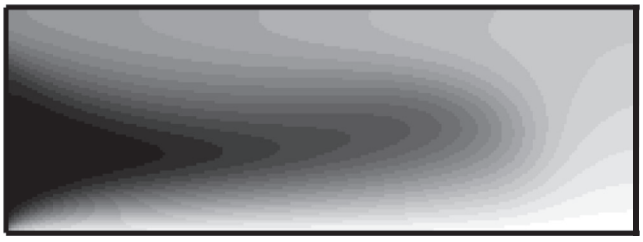

(a) thermal field (present results)

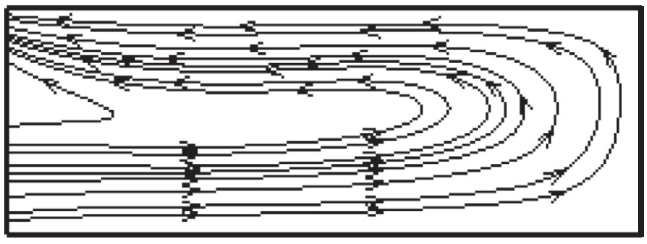

(b) streamlines (present results)

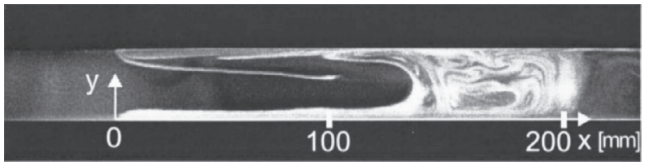

(c) existing results [14]

Fig. 11. Comparison of flow fields of present results and existing results [14].

$Ra^* = 2.18 \times 10^6$, the appearance of the smallest time-averaged local Nusselt number in the central region is observed and reasonable.

Flow visualization of existing results of [14] compared with present results are shown in Fig. 11. Near the central line, a region where fluids turn flowing directions is found out. Both results have a similar tread.

A comparison of time and area averaged Nusselt numbers of present results and existing results is revealed in Fig. 12. The

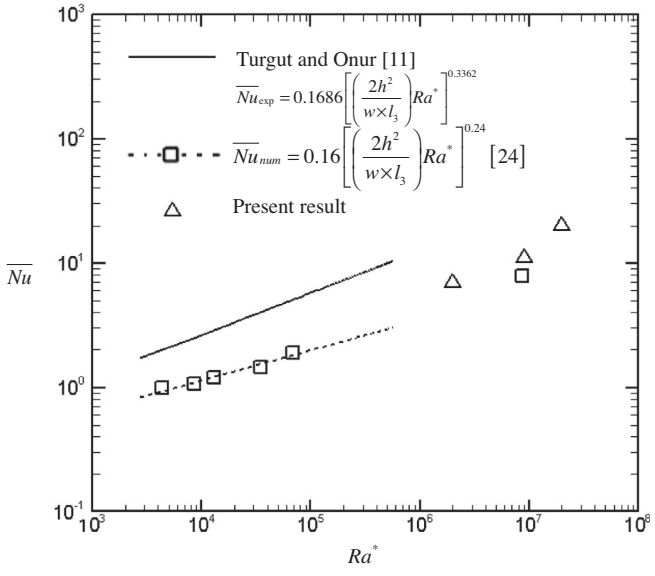

Fig. 12. Comparison of averaged average Nusselt numbers of present results and existing results [11,24].

definition of time and area averaged Nusselt number is shown as follows.

$$\bar{\bar{Nu}} = \frac{1}{d \cdot l}\int_d \int_l \bar{Nu}_x dxdz \tag{32}$$

The reasonable difference between the experimental results [11] and the previous study [24] was reasoned in [24]. The Rayleigh numbers of this work are larger than those in [24], larger time and area averaged Nusselt numbers are then achieved. The slope of the distribution of the present results is slightly larger than the slope of the extension line of the results of [24]. The reason is suggested as that unstable phenomena easily happen in situations of the large Rayleigh numbers.

5. Conclusions

An investigation of effects of heights and a length on natural convection of three dimensional parallel plates with a heated bottom surface is studied numerically. Phenomena of this work are deeply affected by the height and length, and different from those observed in the previous study [24]. Several conclusions are drawn as follows.

(1) The space used for developing natural convection plays an important role to dominate phenomena of natural convection. In a narrow space, phenomena trend to a stable situation, and vice versa.
(2) A T-shape roll cell is a kind of intermediate product and observed in an earlier stage of the growth of natural convection under a certain height in this work.

Acknowledgments

The authors gratefully acknowledge the support of the Natural Science Council, Taiwan, ROC under Contact NSC99-2221-E-009-058.

References

[1] L.Q. Tang, T.T.H. Tsang, Temporal, spatial and thermal features of 3-D Rayleigh–Bénard convection by a least-squares finite element method, Comput. Methods Appl. Mech. Eng. 140 (1997) 201–219.
[2] H. Yang, Z. Zhu, Numerical simulation of turbulent Rayleigh–Benard convection, Int. J. Heat Mass Transfer 33 (2006) 184–190.
[3] B.A. Puthenveettil, A. Jaywant H, Plume structure in high-Rayleigh-number convection, J. Fluid Mech. 000 (2005) 1–33.
[4] M. van Reeuwijk, H.J.J. Jonker, K. Hanjalić, Wind and boundary layers in Rayleigh–Bénard convection. I. Analysis and modeling, Phys. Rev. E 77 (2008) 036311.
[5] W. Aung, L.S. Fletcher, V. Sernas, Developing laminar free convection between vertical flat plates with asymmetric heating, Int. J. Heat Mass Transfer 15 (1972) 2293–2308.
[6] P.H. Oosthuzien, A numerical study of laminar free convective flow through a vertical open partially heated plane duct, ASME HTD 32 (1984) 41–48.
[7] S. Kim, N.K. Anand, W. Aung, Effect of wall conduction on free convection between asymmetrically heated vertical plates: uniform wall heat flux, Int. J. Heat Mass Transfer 33 (1990) 1013–1023.
[8] D. Naylor, J.M. Floryan, J.D. Tarasuk, A numerical study of developing free convection between vertical parallel plates, Trans. J. Heat Mass Transfer ASME 113 (1991) 620–626.
[9] A. La Pica, G. Rodono, R. Volpes, An experimental investigation on natural convection of air in a vertical channel, Int. J. Heat Mass Transfer 36 (1993) 611–616.
[10] K. Kitamura, T. Asakawa, Fluid flow and heat transfer of natural convection over upward-facing, horizontal, heated plate shrouded by a parallel insulated plate, Heat Transfer Asian Res. 29 (2000) 333–346.
[11] Oğuz Turgut, Nevzat Onur, An experimental and three-dimensional numerical study of natural convection heat transfer between two horizontal parallel plates, Int. J. Heat Mass Transfer 34 (2007) 644–652.
[12] H. Yang, Z. Zhu, J. Gilleard, Numerical simulation of thermal fluid instability between two horizontal parallel plates, Int. J. Heat Mass Transfer 44 (2001) 1485–1493.

[13] O. Manca, B. Morrone, S. Nardini, Experimental analysis of thermal instability in natural convection between horizontal parallel platesuniformly heated, J. Heat Transfer 122 (2000) 50–57.
[14] O. Manca, S. Nardini, Experimental investigation on natural convection in horizontal channels with the upper wall at uniform heat flux, Int. J. Heat Mass Transfer 50 (2007) 1075–1086.
[15] S. Baskaya, H. Kauli, Effects of plate separation, plate length and temperature difference on buoyancy driven heat transfer in finite horizontal parallel plates, Heat Mass Transfer 40 (2004) 293–330.
[16] J.F. Hinojosa, C.A. Estrada, R.E. Cabanillas, G. Alvarez, Numerical study of transient and steady-state natural convection and surface thermal radiation in a horizontal square open cavity, Numer. Heat Transfer A 48 (2005) 179–196.
[17] T. Icoz, Y. Jaluria, Numerical simulation of boundary conditions and the onset of instability in natural convection due to protruding thermal sources in an open rectangular channel, Numer. Heat Transfer A 48 (2005) 831–847.
[18] F. Penot, Numerical calculation of two-dimensional natural convection in isothermal open cavities, Numer. Heat Transfer 5 (1982) 421–437.
[19] K. Vafai, J. Ettefagh, The effect of sharp corners on buoyancy-driven flows with particular emphasis on outer boundaries, Int. J. Heat Mass Transfer 33 (1990) 2311–2328.
[20] K. Khanafer, K. Vafai, Buoyancy-driven flows and heat transfer in open-ended enclosures: elimination of the extended boundaries, Int. J. Heat Mass Transfer 43 (2000) 4087–4100.
[21] K. Khanafer, K. Vafai, Effective boundary conditions for buoyancy-driven flows and heat transfer in fully open-ended two-dimensional enclosure, Int. J. Heat Mass Transfer 45 (2002) 2527–2538.
[22] A. Andreozzi, Y. Jaluria, O. Manca, Numerical investigation on transient natural convection in a horizontal channel heated from upper wall, Numer. Heat Transfer A 51 (2007) 815–842.
[23] A. Andreozzi, O. Manca, Numerical investigation on the steady state natural convection in a horizontal open-ended cavity with a heated upper wall, Numer. Heat Transfer A 57 (2010) 453–472.
[24] W.S. Fu, W.H. Wang, S.H. Huang, An investigation of natural convection of three dimensional horizontal parallel plates from a steady to an unsteady situation by a CUDA computation platform, Int. J. Heat Mass Transfer 55 (2012) 4638–4650.
[25] P.L. Roe, Approximation Riemann solver, parameter vectors, and difference schemes, J. Comput. Phys. 43 (1981) 357–372.
[26] J.M. Weiss, W.A. Simth, Preconditioning applied to variable and constants density flows, AIAA 33 (1995) 2050–2056.
[27] X.F. Xu, J.S. Lee, R.H. Pletcher, A compressible finite volume formulation for large eddy simulation of turbulent pipe flows at low Mach number in Cartesian coordinates, J. Comput. Phys. 203 (2005) 22–48.
[28] W.S. Fu, C.G. Li, C.C. Tseng, An investigation of a dual-reflection phenomenon of a natural convection in a three dimensional horizontal channel without Boussinesq assumption, Int. J. Heat Mass Transfer 53 (2010) 1575–1585.
[29] S. Yoon, A. Jamesont, Lower–upper symmetric-gauss–Seidel method for the Euler and Navier–Stokes equations, AIAA 26 (1988) 1025–1026.
[30] I. Abalakin, A. Dervieux, T. Kozubskaya, A vertex centered high order MUSCL scheme applying to linearised Euler acoustics, INRIA No 4459 (2002).
[31] T.J. Poinsot, S.K. Lele, Boundary conditions for Navier–Stokes, J. Comput. Phys. 101 (1992) 104–129.
[32] NVIDIA CUDA Compute Unified Architecture 3.0 programming Guide, NVIDIA Corporation, 2010.